Microstructural impact on flank wear during turning of various Ti-6Al-4V alloys

Dinh Nguyen[a], Di Kang[b], Thomas Bieler[b], Kyunghee Park[c], Patrick Kwon[a],*

[a] Department of Mechanical Engineering, Michigan State University, East Lansing, MI, United States
[b] Department of Chemical Engineering and Materials Science, Michigan State University, East Lansing, MI, United States
[c] Korean Institute of Industrial Technology, 89 Yangdaegiro-gil, Ipjang-myeon, Seobuk-gu, Cheonan, ChungNam 331-822, Republic of Korea

ABSTRACT

Titanium alloys typically do not contain hard inclusion phases typically observed in other metallic alloys. However, the characteristic scoring marks and more distinctive micro- and/or macro-chippings are ubiquitously observed on the flank faces of cutting tools in machining titanium alloys, which is the direct evidence of abrasive wear (hard phase(s) in the microstructure abrading and damaging the flank surface). Thus, an important question lies with the nature of the hard phases present in the titanium microstructure. In this work, we present a comprehensive study that examines the microstructural impact on flank wear attained by turning various Ti-6Al-4V bars having distinct microstructures with uncoated carbide inserts. In particular, four samples with elongated, mill-annealed, solution treated & annealed and fully-lamellar microstructures were selected for our turning experiments. After turning each sample, the flank surface of each insert was observed with confocal laser scanning microscopy (CLSM) and analyzed to determine the flank wear behavior in relation to each sample' distinct microstructures. To characterize the microstructure, scanning electron microscopy (SEM) together with Orientation imaging microstructure (OIM) was used to identify and distinguish the phases present in each sample and the content and topography of each phase was correlated to the behavior of flank wear. The flank wear is also affected by the interface conditions such as temperature and pressure, which were estimated using finite element analysis (FEA) models. The temperature dependent abrasion models enable us to estimate the flank wear rate for each microstructure, and are compared with the experimentally measured wear data.

1. Introduction

Titanium (Ti) and its alloys are extensively used because of their high strength-to-weight ratio, high operating temperature, and fracture and corrosion resistance. Ti alloys are considered light metal alloys along with aluminum (Al) and magnesium (Mg) with its density at 4.3 g/cm^3 [1,2], which is higher than Al and Mg but only about 60% of the density of steel (7.83 g/cm^3). Ti alloys have tensile strengths equivalent to ferrous alloys [1,3]. Another advantage of Ti alloys is its capability to withstand high temperatures. For example, the parts made of Al alloys can operate up about 130 °C [4,5] compared to Ti alloys which can operate well above 300 °C [6]. Some Ti alloys can work well under operating temperature as high as 595 °C [3,4]. Because of these excellent characteristics, Ti alloys are extensively used in medical, food and chemical applications [5–7]. Like other metallic alloys, Ti alloys are castable, forgeable, and weldable with many conventional techniques. However, the high cost of Ti alloys, about four times of that of stainless steel, is the main obstacle in utilizing Ti alloys in many other possible applications [3]. In addition, the

machinability of Ti alloys is very poor and not well understood in spite of the extensive research work since 1960s. The poor machinability of Ti alloys comes from relatively low stiffness, high strength even at high temperature and the low thermal conductivity. For example, the most common Ti alloy, Ti-6Al-4V (or Ti64), has the low thermal conductivity at 6.7 W/m-K (compared to 50 W/m-K for 1045 steel) and the hardness between 30 and 36 GPa [3,8].

Ti alloys consist of two main crystal structures, hexagonal close packed (HCP or α) and body-centered cubic (BCC or β) structures that depend on the alloying elements and heat treatment. Accordingly, they are classified into four groups, commercially pure (CP) α, near α, α-β and metastable β. The CP α-Ti has excellent corrosion resistance, but it has a low strength and limited working temperature only up to 300 °C. The α and near-α alloys such as Ti-5Al-2.5Sn and Ti-8Al-1Mo-1V contain α-stabilizing elements (Al) with small amounts of β-stabilizing elements (Mo, V), which enable them to operate up to 520 °C. They have a good weldability but poor forgeability compared to α-β alloys. Ti64 is the most common Ti alloy and belongs to the α-β group with 5.5–6.75% Al, and 3.5–4.5% V. With appropriated heat treatments,

---

* Corresponding author.

they are used in high-strength applications, and have application temperatures up to 400 °C. The metastable β alloys have high fractions of β-stabilizers present and have high hardenability and forgeability [3,6].

The microstructures of Ti alloys can be various combinations of α and β-phases, which can be formed by alloying with other elements and heat treatment. In addition to the individual α- and β-grains, the lamellar phase is very common, which have a basket-weave structure of α and β phases [1,9]. Ti64, for example, can have various distinct microstructures, fully-equiaxed, mill-annealed, solution treated and aged (STA) or lamellar (also referred to as fully lamellar) by adjusting the thermo-mechanical processing [3,10]. For example, the STA microstructure can be obtained by the following process: homogenization above the β-transus of 955 °C followed by hot deformation with recrystallization and aging at 500 °C [11]. The heat process with mill-annealed condition is similar to the STA heat treatment but without recrystallization. The difference between fully equiaxed and STA microstructures is the recrystallization temperature or cooling rate [8]. To form the fully lamellar microstructure, the heat treatment starts with homogenization above β-transus temperature and slow cooling. As the material gradually cools below the β-transus, the α-phase nucleates in numerous parallel plates on particular planes in β-phase, resulting in distinct but irregularly shaped colonies of the lamellar microstructure. The lamellar spacing becomes larger with slower cooling rates. As the colonies can nucleate on six different planes of the β-phase, multiple colonies nucleate in different parts of a prior β-grain with different lamellar orientations. Within a prior β-grain, several different colonies form with different α-orientations, which gives a basket weave appearance, but the remaining minority β-phase in each of these colonies has the same orientation.

Ti alloys are known to have poor machinabilities due to several characteristics. For example, the low modulus of Ti alloys makes the machining process prone to the machining instability and the low thermal conductivity elevates the temperature at the cutting zone. Dearnley et al. [12] estimated the cutting temperature on the rake face to reach 900 °C when turning Ti64 at 75 m/min, 0.25 mm/rev in 10 s with cemented carbides tools. Because the cutting temperature is high with an extremely small heat-affected zone (also due to the low thermal conductivity), extensive tool wear concentrates around cutting tip and chipping becomes prevalent [6]. More importantly, due to the high chemical reactivity of Ti, most available cutting tools form an adhesion layer that causes attrition wear on the tool and micro/macro fracture when the adhesion layer detaches portion of a tool.

Numerous works have reported the machinabilities of various Ti alloys with a wide range of microstructures. Arrazola et al. [13] carried out turning experiments up to the cutting speed of 100 m/min to compare the machinabilities of Ti555.3 (solution-treated and aged (STA)) and Ti64 (quenched and annealed) with uncoated cemented carbide tools. The microstructure of Ti64 had 80% of α-phase and 20% lamellar phase while Ti555.3 has 20% of α-phase and 80% lamellar phase. The flank wear results showed that the machinability of Ti555.3 was extremely poor compared to that of Ti64. Khanna et al. [14] conducted an orthogonal dry machining experiment and measured the cutting temperature with an infrared camera on mill-annealed Ti64 and three Ti54M bars with distinct microstructures, mill-annealed, STA and lamellar. The cutting temperature reached up to 1000 °C when cutting at 80 m/min. The cutting temperatures were reported to be similar among the bars and to be very sensitive to the feed rate. Armendia et al. [15] reported that the machinability of Ti54M was better than Ti64 when machining with uncoated carbide tools. Both work materials in the experiment had similar mechanical properties despite of distinct heat treatment conditions. The Ti64 microstructure had coarse α-Ti laths with lamellar spacing of 20 μm whereas Ti54M had finer microstructure with the average size of 10 μm. Ti64 also has a higher fraction of equiaxed α-grains than Ti54M. They concluded that the machinability of Ti54M was approximately 10–15% better than Ti64 at their

maximum cutting speeds (90 m/min for Ti54M and 80 m/min for Ti64). The cutting and feed forces were measured with a piezoelectric sensor, and both forces were about 100 N/mm^2 lower for Ti54M than those of Ti64. Kosaka et al. [16] have also studied the drilling machinability of three Ti alloys, Ti5Al4V-low Mo/Fe, Ti5Al4V-high Mo/Fe and Ti64 mill-annealed. Based on the microstructure images (and the Al content), the amount of primary α-phase in Ti64 is higher than the other two, and the size of primary α-grains of Ti5Al4V-high Mo/Fe was larger than Ti5Al4V-high Mo/Fe. The results showed that Ti64 was more difficult to machine than the other two. Comparing between Ti64 and Ti54M, Ti64 had more lamellar structure and poorer machinability than Ti54M.

Attanaiso et al. [17] studied Ti64 with four distinct microstructures: full equiaxed, mill-annealed, bi-modal and fully lamellar by micro-milling with a cutting speed of 15.7 m/min and feed rate of 0.5 and 1.5 μm/tooth. The bi-modal has the highest hardness at 411 ± 15 Hv and the lamellar structure had the lowest micro-hardness at 356 ± 45 Hv whereas the hardness of lamellar structures measured with the nanoindentation is much smaller than equiaxed α grains. The cutting force was the lowest with the lamellar microstructure at the feed rate of 1.5 μm/tooth. Gelfi et al. [18] reported the cutting forces when machining Ti64 with varying characteristics of the lamellar phase. The different lamellar structures were generated by heating up to 1020 °C, 1050 °C and 1080 °C followed by either furnace or air cooling. The microstructure obtained by cooling in furnace is coarser in colony size and finer in lamellae width than cooling in air. The hardness was increased by cooling in air. However, the cutting force is lower with air cooling than furnace-cooled. The cutting force reduces significantly as the lamellar colony becomes coarser and the width of each lamella becomes finer. Dearnley et al. [12] carried out the machining experiment on the elongated microstructure of Ti64 with three distinct categories of available inserts including uncoated and coated carbides and ceramics. They suggested the most suitable insert was uncoated carbides (with 6w% cobalt) and borides shows the excellent resistance to crater wear (solubility). Birmingham et al. [19] compared on the flank wear after turning the lamellar Ti64 with carbide inserts under dry and cryogenic coolant conditions using one cutting speed of 125 m/min with the feed rate of 0.15, 0.2 and 0.36 mm/rev and the depth of cut of 1.1, 2.0 and 2.7 mm. The lamellar microstructure has the α-lath thickness of 5 μm and lamellar grain size of approximate 1 mm. The combination of low feed rate and high depth of cut improved tool life substantially.

Some works focused on experimentally measuring the cutting temperature. Narutaki et al. [20] measured the cutting temperature using the thermocouple technique. The cutting temperature reached up to 727 °C at 60 m/min and about 1077 °C at 200 m/min when cutting Ti64 and Ti5Al2.5Sn with carbide tools. Kitagawa et al. [21] carried out milling and turning experiments with Inconel 718 and Ti6Al6V2Sn to measure the cutting temperature with the thermocouple mounted into the through-hole of the inserts. The cutting temperature when turning Ti6Al6V2Sn (α + β Ti alloy) at the cutting speed up 200 m/min with K-10 carbide inserts was 1050 °C. Zoya et al. [22] studied α + β Ti alloys with 4.5%Al and 4.5%Mn with a lamellar microstructure. Turning experiments with cBN tools were conducted at the cutting speeds of 185, 220 and 280 m/min. The cutting temperatures measured with a non-contact-type IR pyrometer and were reported to range between 500 °C and 1000 °C depending on the cutting speed.

The work of Attanaiso et al. [17] reported on the differences in cutting force among four distinct microstructures of Ti64 without any implication on the machinability or more specifically tool wear as the experiment took place under micromilling process. This paper intends to examine the effect of various microstructures on flank wear by turning four distinct samples of Ti64, elongated (ELO), mill-annealed (MIL), solution treated and aged (STA) or lamellar (LAM). The ELO microstructure is one variation of a fully-equiaxed microstructure, which can be obtained with rolling processes. These four microstruc-

Table 1
Overall dimensions of Ti64 round bars.

Sample	Diameter (cm)	Length (cm)
Elongated (ELO)	12.7	50.2
Mill-anneal (MIL)	12.7	35.6
Solution Treated & Annealed (STA)	12.7	64.8
Lamellar (LAM)	12.7	35.6

tures provide a range of variation in the content of α-phase and the corresponding lamellar phase, which enable us to determine the impact of these phases on flank wear when turning with carbide inserts. The dry turning experiment is conducted to observed the difference in flank wear impacted by each phase. The abrasive wear models were used to explain the observed flank wear with the help of finite element simulation to estimate the cutting temperature.

2. Experimental procedures

2.1. Turning experiments

Turning experiments were conducted with four distinct Ti64 cylindrical bars whose microstructures are ELO, MIL, STA and LAM with the overall dimensions as shown in Table 1. The straight turning process was carried out in a dry condition with Daewoo PUMA 300L CNC turning center (manufactured by Doosan Machine Tools, Seoul, South Korea). Each sample was turned at three distinct surface speeds of 61, 91 and 122 m/min. The depth of cut and feed rate were kept constant at 1.2 mm and 0.127 mm/rev, respectively. These conditions are recommended by Sandvik Coromant for the cutting inserts chosen for this study.

Uncoated carbide inserts, H13A grade with super fine grain size (the average grain size of 1 μm) and 6 wt% of cobalt, were supplied by Sandvik Coromant (Herbon, KY). The rake and relief angles were 0° and 7°, respectively. The geometry parameters are ANSI designation CNMA-432 without chip breaker and the thermal conductivity of the carbide is 65 W/m K, as shown in Table 2.

2.2. Flank wear measurement

After machining, 52% hydrofluoric acid (HF) was used to etch the adhesion layer deposited on the inserts during cutting. The flank wear was measured using 3D laser scanning microscopy (VK-X100 manufactured by Keyence corporation, Osaka, Japan) by Korean Institute of Industrial Technology (KITECH). The 3 dimensional (3D) geometry of the flank wear land was generated by capturing the reflection from the

focal volume on the focal plane and the optical images. The turning process was interrupted after machining for a given time to retrieve the worn inserts and install a new insert before subsequent machining. Thus, the flank wear on each corner was saved, which enable use to quantitatively determine flank wear as a function of time (or cutting length).
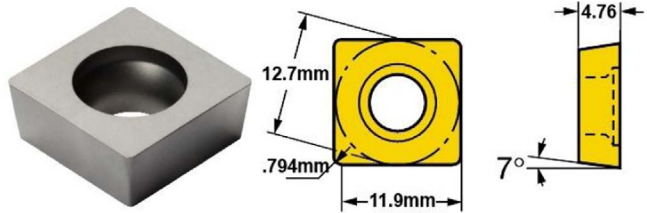
2.3. Microstructures of Ti-work materials

The microstructures attainable with Ti64 can range from mostly α-phase to completely lamellar phase (thin β lamellae between laths of α in colonies with the same crystal orientations making a basket-weave like pattern). This paper assesses the effect of each phase and its size, shape and spatial arrangement on machining of Ti alloys. From this work, rationale for recommending the optimal microstructure to attain the best machinability in Ti64 (as well as other Ti alloys containing these two phases) will be proposed to avoid any expensive machining for particular microstructure of Ti64.

Both α and lamellar phases are identified to be the important factors in machining. Our previous work [23,24] showed that the root cause of flank wear when turning the elongated (ELO) microstructure (Fig. 1(a)) was identified as the hard orientation of the anisotropic α-crystals or cluster (as a group of neighboring α-crystals in a similar orientation denoted as 'hard α') which must be defined in relation to the cutting direction. However, as evident in Birmingham et al. [19], Ti64 with the fully lamellar phase had even poorer machinability. Thus, to understand the machinability of various microstructures of Ti64 alloys, we conducted a series of turning experiments on Elongated (ELO), Mill-anneal (MIL), Solution Treated and Aged (STA) and Lamellar (LAM) of Ti64, which provide a wide range of microstructures with the distinct content and arrangement of the α and lamellar phases. Please note that the ELO microstructure is resulting from unidirectional working of the equiaxed microstructure.

The microstructure of each sample was examined with Scanning Electron Microscopy (SEM) as shown in Fig. 1 (20 keV, 9 mm working distance, 1000× magnification in backscattered electron imaging mode using a Jeol 6610LV SEM). The backscattered electron yield at the detector is stronger from the β-phase, which appears as a lighter or white shade, which allows detection of the β-grains and the β-phase in lamella colonies. More importantly for the α-phases, the orientation of the α-grains was measured with Electron-Backscattered Diffraction (EBSD) scans with a MIRA SEM (Tescan, Orsay Holding, Kohoutovice, Czech Republic) with an Ametek (TSL) orientation imaging microscopy (OIM) system. EBSD scans were obtained on the area of 800×800 μm with 2 μm step size to detect the crystal orientation of the α-grains.

The crystal orientation was measured on the interior part of the bar as described in Fig. 2 in order to avoid the microstructures affected by

Table 2
Parameter summary for uncoated carbide tool.

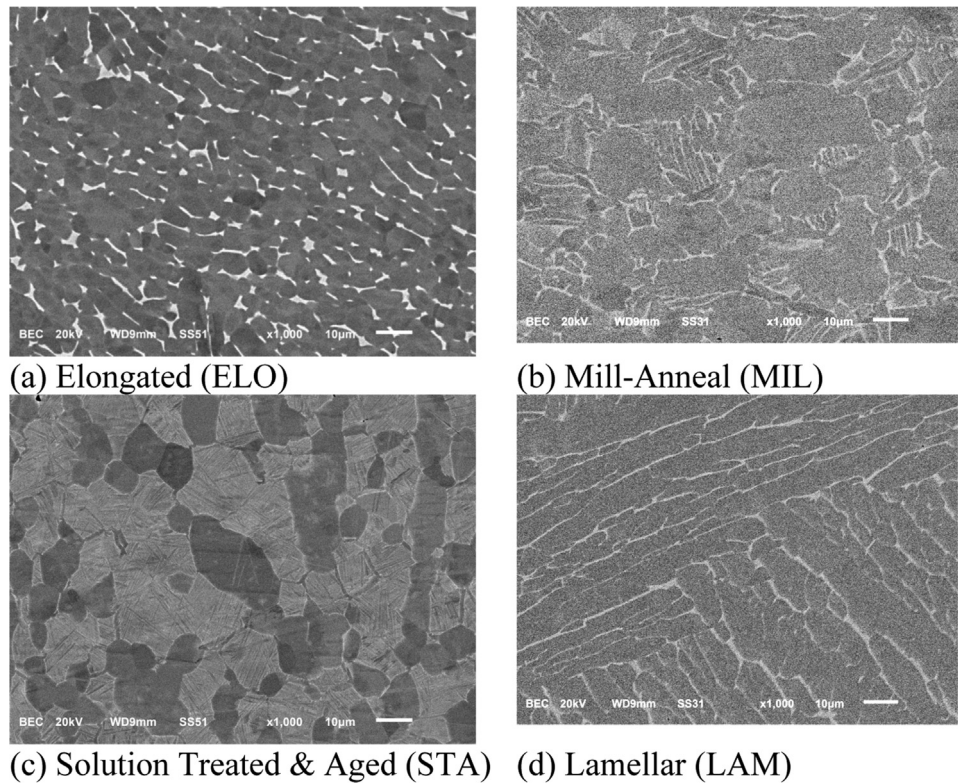| Grade	H13A
Substrate	WC+6%Co
Thermal conductivity	65 W/m.K
Dimension	
Supplier	Sandvik Coromant

Fig. 1. Microstructural images of Four Ti64 bars used in the machining study.

the surface of the rolling process and other surface abnormalities. For each bar, the microstructures, both α-cluster and lamella colony characteristics were identified and examined to estimate the arrangement and sizes of hard α cluster and lamellar colonies. Thus, before performing turning experiments, a piece of each bar was cut out from the round bar as shown in Fig. 2(a). Each sample was cut with wire electrical discharge machine (EDM) to preserve their original microstructures and further polished to remove any EDM surface artifact. The microstructure on each face (Top, Front or Side) was measured to identify the crystal orientations of α-grains and the size of the hard α-clusters as shown in Fig. 2(b). Because of the location of the cutout sample from each bar shown in Fig. 2(a), the hard α-crystals on each face of the sample were defined as shown in Fig. 2(b). The microstructures on all three faces were exposed on our metallurgical mount as shown in Fig. 2(c). Table 3 shows the average sizes of the α-grains and lamellar colonies in each sample. The size of individual α-grain is the smallest at 8.11 μm in the ELO sample and the largest at 15.3 μm in the MIL sample.

3. Results and discussion

The α-grain in the microstructure is highly anisotropic, exhibiting strong anisotropic mechanical properties as Britton et al. [25] claimed the hardness and elastic modulus are substantially higher on the surface whose normal vector aligning with the c-direction of α-crystals than any other surface. Specifically, it is about 20% higher in hardness (560 Hv compared to 459 Hv). The hardness as a function of the declination angle, defined by the deviation from the c-direction of an α-crystal, does not change substantially between 0° and ± 20° and, thus, the cluster of crystals with the declination angle of ± 20° from the cutting direction are defined to be the hard α-cluster or 'hard α'. The α-phase exists as individual phase as well as part of lamellar phase with alternating layers of thick α and thin β phase. These crystals are randomly oriented throughout its microstructure. The orientation of each α-crystal in our microstructures was measured using the Orienta-

tion Imagine Microscopy™ (OIM). The OIM scans provide orientation maps of the α–grain orientations of three of the four Ti64 samples, ELO, STA and MIL samples. The LAM sample has very large lamella colonies, such that no more than a few partial colonies are present in a similar sized OIM map. The images from OIM shown Fig. 3(a) present partial crystal orientation information of each grain, which is represented by different colors. The α-grains clearly exist as clusters where multiple neighboring grains have a similar crystal orientation. We hypothesize that flank wear is generated by the abrasive action by these 'hard' clusters [23,24], for example, in the ELO sample. From the OIM images, the orientation and shape of hard clusters in relation to the cutting direction were extracted. For example, the red regions represent the α-clusters in the hard orientation in relation to the cutting direction. These hard regions are extracted from Fig. 3(a) and presented in Fig. 3(b). Fig. 3 contains the three OIM images from three distinct views (Top, Front and Side (see Fig. 2(b)) to demonstrate the anisotropic texture in the MIL microstructure) and the OIM images of the front views of ELO and STA. The average sizes of the hard clusters were analyzed using the Gauss filter [26] and the contours of hard clusters were generated for the ELO, MIL and STA samples on each of the three views (Side, Top and Side) in order to identify the hard α-phase in relation to cutting direction.

Table 4 summarizes the area fractions of α and β phases. Details of our estimation scheme will be presented in the next section. The ELO sample does not have any lamellar content while the LAM sample does not contain distinct α phase, despite the fact that all four samples have a similarly high content (around 99%) of α phase (this is an upper bound, as it is difficulty to capture the finest β phase). All of the α phase resides as part of the lamellar constituent in the LAM sample while all of the β phase resides as individual grains in the ELO sample. Only a small fraction of the α phase is hard and contributes to severe flank wear. Averages of the area fractions obtained from each face shown in Fig. 2 are shown in Table 4.

Table 5 presents the estimated average size of hard α clusters on each of three faces for the ELO, STA, and MIL samples. Based on the
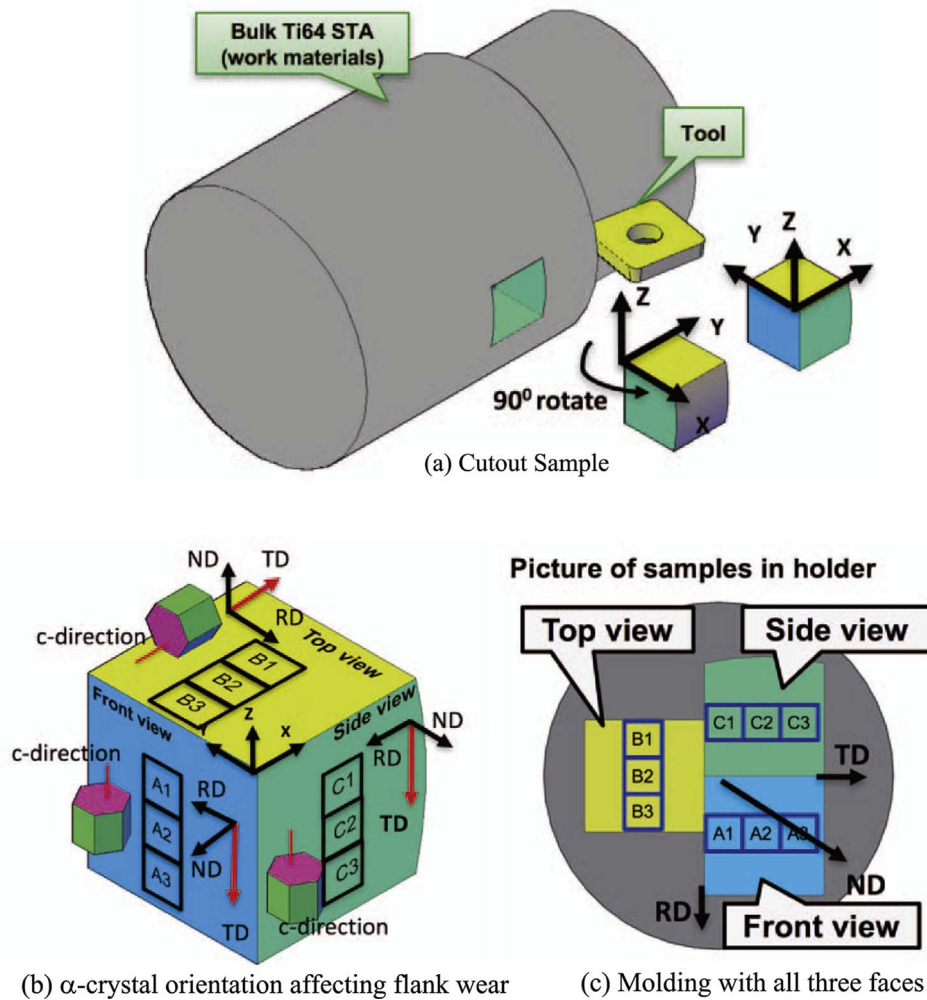
(a) Cutout Sample

(b) α-crystal orientation affecting flank wear

(c) Molding with all three faces

Fig. 2. Microstructure images of Ti64 bars.

Table 3
Average size for each constituent phase in four samples.

Ti64	ELO	MILL	STA	LAM
Average Size of α-grains (μ)	8.11	15.3	10.2	–
Average size of lamellar colonies (μ)	–	22.0	19.7	743.1

microstructures on the three faces, the hard cluster size can be estimated in three directions representing length, width and height, which is presented as an ellipsoidal shape for α-clusters as shown in Fig. 3. Please note that the ellipsoid does not represent the shape of hard entities which are traditionally perceived as the abrasives. It is the dimensional representation of the hard clusters with three characteristic dimensions, Length, Width and Height. The lamellar phase could not be represented as ellipsoidal shape as the microstructure of three faces could not be correlated. The LAM sample had the largest colony size of 743 μm and the other two samples with lamellar colonies each had a similar lamellar colony size of around 20 μm (Fig. 4).

3.1. The contents of lamellar and hard α-clusters in each sample

The BSE images were used to distinguish the lamellar regions from the α-phases. The α-phase is the uniformly dark phase while the β phases are bright, as shown in Fig. 5(a) and (d) and Fig. 1. Fig. 5 shows the SEM images of the MIL (a)–(c) and STA samples (c)–(e) that contain 11.9% and 57.1%, lamellar structure, respectively and the SEM image and EBSD image of the LAM sample (f)–(g). The EBSD does not provide

refined enough images to detect the thin β-phase within each colony. The EBSD image show the orientation of the much larger α-grains which have the same orientation within each colony. The lamellar content as well as α-content is summarized for our four samples in Table 2. Some of the equiaxed α grains are in the hard orientation. The four samples have a wide range of lamellar content (between 0% and 100%) but a small range of the hard α phase (between 3.37% and 4.4%). The average lamellar size of MIL, STA and LAM samples was measured from SEM images as illustrated in Fig. 5 and summarized in Table 3.

The microhardness was measured on each sample using a CM-800AT, Sun-Tec Microhardness testing system with the test load of 500 gf and 15 s of dwell time with 50× objective. The indentation matrix of 6 columns by 5 rows (total 30 indentations) was applied with the spacing of 250 μm at room temperature. Table 6 summarizes the hardness values of the four samples. Overall, the STA sample had the highest hardness at 331.9 Hv whereas LAM sample had the lowest hardness at 297.7 Hv. These values did not agree well with the hardness measured by Attanasio et al. [17] who reported substantially higher values. Their report indicated that the STA sample had the highest microhardness of 411 Hv whereas the LAM sample had the lowest value of 356 Hv. However, the trends in hardness values among the four samples are in a good agreement.

3.2. Flank wear

Among many machinability measurements such as the material

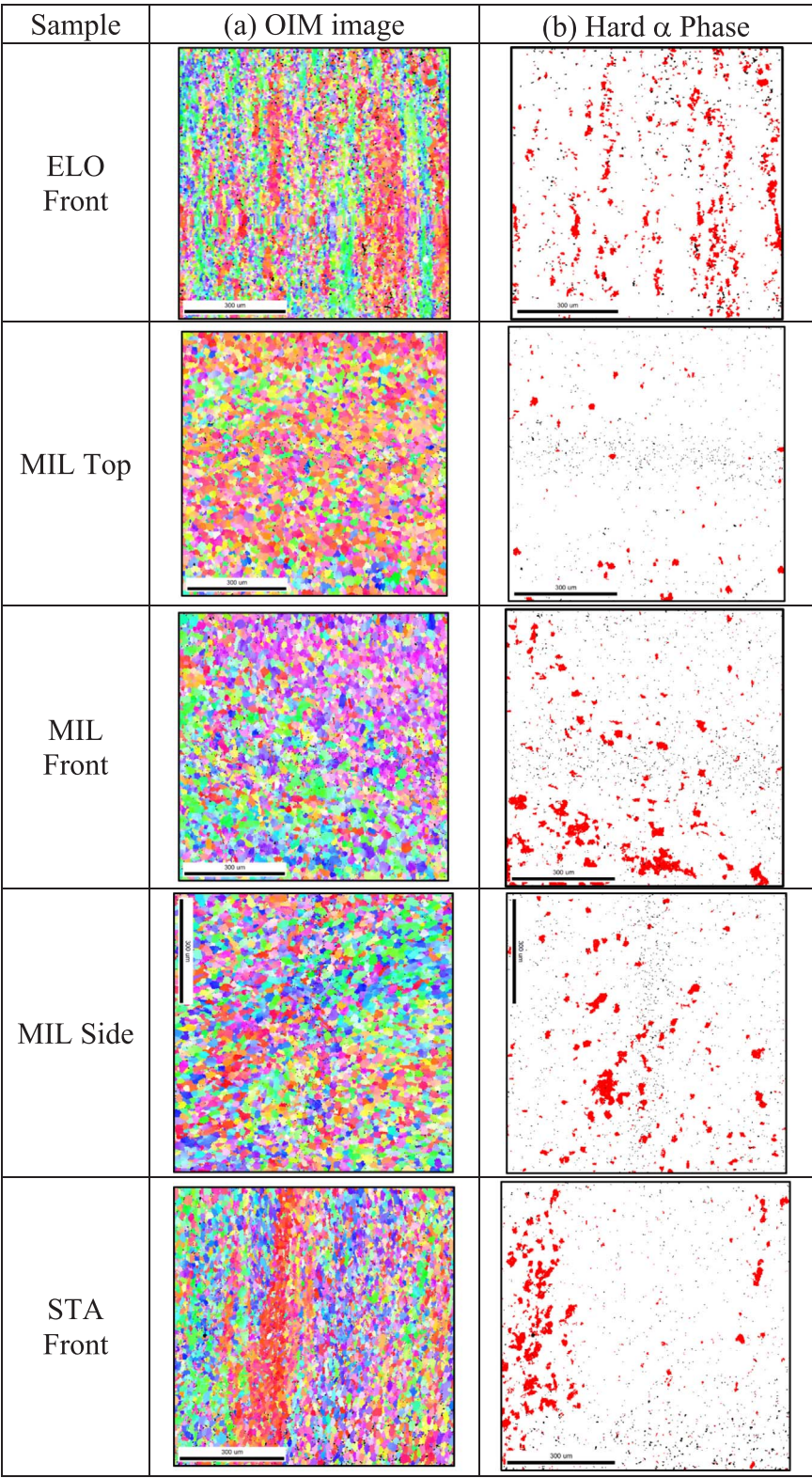| Sample	(a) OIM image	(b) Hard α Phase
ELO Front		
MIL Top		
MIL Front		
MIL Side		
STA Front		

Fig. 3. Microstructural orientation analysis of ELO, MIL, STA and LAM samples.

removal rates, cycle time and tool wear, flank wear is the most commonly used method to quantify the machinability. Fig. 6 presents the flank wear captured by 20× magnification after etching with HF solution after turning at each of the three cutting speeds, 61, 122 and 122 m/min. As the cutting speed increases, the flank wear obviously increases for each sample. The main feature of flank wear in all four samples at the cutting speed of 61 m/min was that the scoring marks are not pronounced until more than 330 m were cut. The trends in flank wear at the low cutting speed were similar in all four samples of Ti64 as shown in Fig. 6(a). At the cutting speed of 61 m/min, the flank wear was slightly higher as the lamellar fraction increases. At the cutting speed of 91 m/min, the scoring marks after cutting each sample are clearly formed marks even at the initial stages of flank wear while they become more apparent and wider in the later stages as shown in

Table 4
Area fraction of each phase present in each sample.

	ELO	MIL	STA	LAM
α phase (SEM)	98.6%	99.2%	99.2%	99.6%
Hard α phase	**4.4%**	**3.83%**	**3.37%**	**0%**
β phase (SEM)	1.4%	0.8%	0.8%	0.4%
Equiaxed α grains	98.6%	88.1%	42.9%	0%
Lamellar Colonies	**0%**	**11.9%**	**57.1%**	**100%**

Table 5
The size of hard α-cluster.

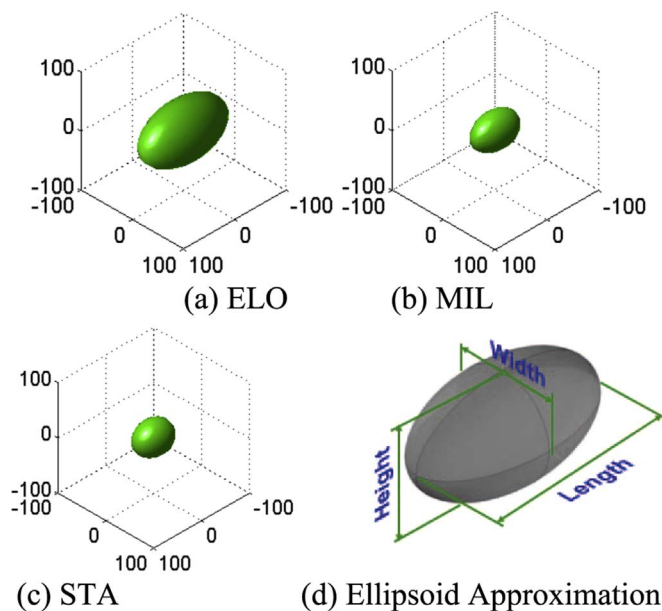| Ti64 samples		Average hard α-cluster size (μ)			
		Min	Max	Ellipsoidal approximation	
ELO	Top	95.98	188.2	Length	160.4
	Front	74.22	132.4	Width	79.0
	Side	83.68	100.7	Height	98.4
STA	Top	54.23	70.31	Length	85.7
	Front	61.75	77.76	Width	50.7
	Side	55.11	59.86	Height	59.5
MIL	Top	47.3	88.9	Length	74.0
	Front	63.49	82.49	Width	54.7
	Side	55.53	54.09	Height	60.8

Fig. 4. Average hard α cluster approximated by an ellipsoid.

Fig. 6(b). The average flank wear increased considerably for all four samples compared to those from the cutting speed of 61 m/min. At the cutting speed of 122 m/min, the scoring marks were clearly formed from the beginning. The width of the scoring marks was much wider than those from the low and middle cutting speeds. The flank wear increased significantly as the content of the lamellar phase increased, as evident with the STA and LAM samples. The flank wear of LAM increased substantially with cutting speed (note the different vertical scales in Fig. 6).

3.3. The scoring mark explanation

The correlation between the scoring marks and the sizes of the hard α-cluster and the lamellar colonies of each sample. As presented in Figs. 3 and 4 and Table 3, each sample has a characteristic size distributions of hard α-cluster and lamellar colonies, which correlate directly with the width of the scoring marks on the flank wear. The hard

α-clusters have dimensional characteristics represented by length, height and width as presented in Table 4. Based on the microstructures in our four samples and the cutting direction, the length of the hard α-clusters observable on the top and front views in Fig. 2 should make the most dominant impact on the width of the scoring marks. The abrasive action will result in the scoring marks such that the width of scoring marks on the flank wear should be smaller or similar to the sizes of the hard cluster and/or the lamellar colonies of each sample. For example, the flank wear image after turning each sample is shown in Fig. 7. With these images, the widths of the scoring marks are collected and analyzed for each sample. The sizes of the hard α-clusters for the three samples (except the lamellar sample) were measured, collected and analyzed from the OIM images shown in Fig. 3(a)–(c) while the average size of the lamellar colonies existing in the three samples (except for the elongated sample) was also measured from the SEM images shown in Fig. 5(c) and (f).

Figs. 8–11 illustrate the correlation between the scoring marks on the flank wear land and the characteristic sizes of both average hard α-cluster and lamellar colony for each of the four samples. From the flank wear images, the width of each scoring mark on the flank wear land was recorded, collected and presented in the histograms. Fig. 8(a) shows the histogram of the widths of the scoring marks on the flank wear lands resulting from cutting the ELO sample at 91 and 122 m/min. The scoring marks from 61 m/min are not apparent for all samples because the scoring marks were too shallow due to the low cutting forces, and not clear enough to measure accurately. The scoring marks from all four samples became more apparent as the cutting speed increased with the increase in the cutting force. The microstructure of the ELO sample consists of (almost 99%) α-grains (see Table 2) of which only about 4.4% are the hard α-clusters causing flank wear. More than 50% of the scoring marks have a width of around 20 μm, which is similar to the size of the hard α-clusters that are mostly between 40 and 100 μm as shown in Fig. 8. Apparently, without any other hard phases, the hard α-clusters are responsible for generating the scoring mark on the flank surface. There are some exceptionally large α-clusters around 200 μm which may have generated the wide scoring marks as large as 50 μm at the cutting speed of 122 m/min.

For the MIL and STA samples, the scoring marks are also correlated with the abrasive actions by both the hard α-clusters and the lamellar colonies. As shown in Fig. 9(a), the scoring mark histogram shows a bimodal distribution in width at both cutting speeds contributed by the distinct size differential between lamellar colonies and hard α-clusters. The combined effect of the hard α-clusters (3.83%) whose average size ranges between 45 μm and 87 μm and the lamellar phase (11.9%) whose average size ranges between 20 and 40 μm, shown in Fig. 10. For the STA sample, the scoring marks with about 10–15 μm at 91 m/min and about 20 μm at 122 m/min are correlated with the higher 57.1% lamellar fraction whose average sizes are about 20 μm, but 3.37% of the hard α-clusters whose average size is approximately 60 μm, as shown in Fig. 10. Because only 3.37% of the total phase is the hard α-cluster contributing to flank wear, the effect of hard α-cluster is minimal.

The LAM sample only has the lamellar colonies, which also produce the scoring marks left on the flank surface. The lamellar colony size in the LAM sample is substantially larger than those and the hard α-clusters of the other three samples. The average of the lamellar colonies is estimated to be around 700 μm. The wide scoring marks whose average width was 300 μm (see Fig. 7) were generated by these large lamellar colonies, shown in Fig. 11. Table 7 presents the summary of the width range of the scoring marks and the sizes of two main phases (hard α-clusters and lamellar colonies) causing flank wear and the correlation between the two is well documented throughout the paper.

3.4. Discussion on flank wear

Fig. 12 represents the flank wear as a function of cutting speed for each sample. For the ELO sample with the hard α-clusters as the main
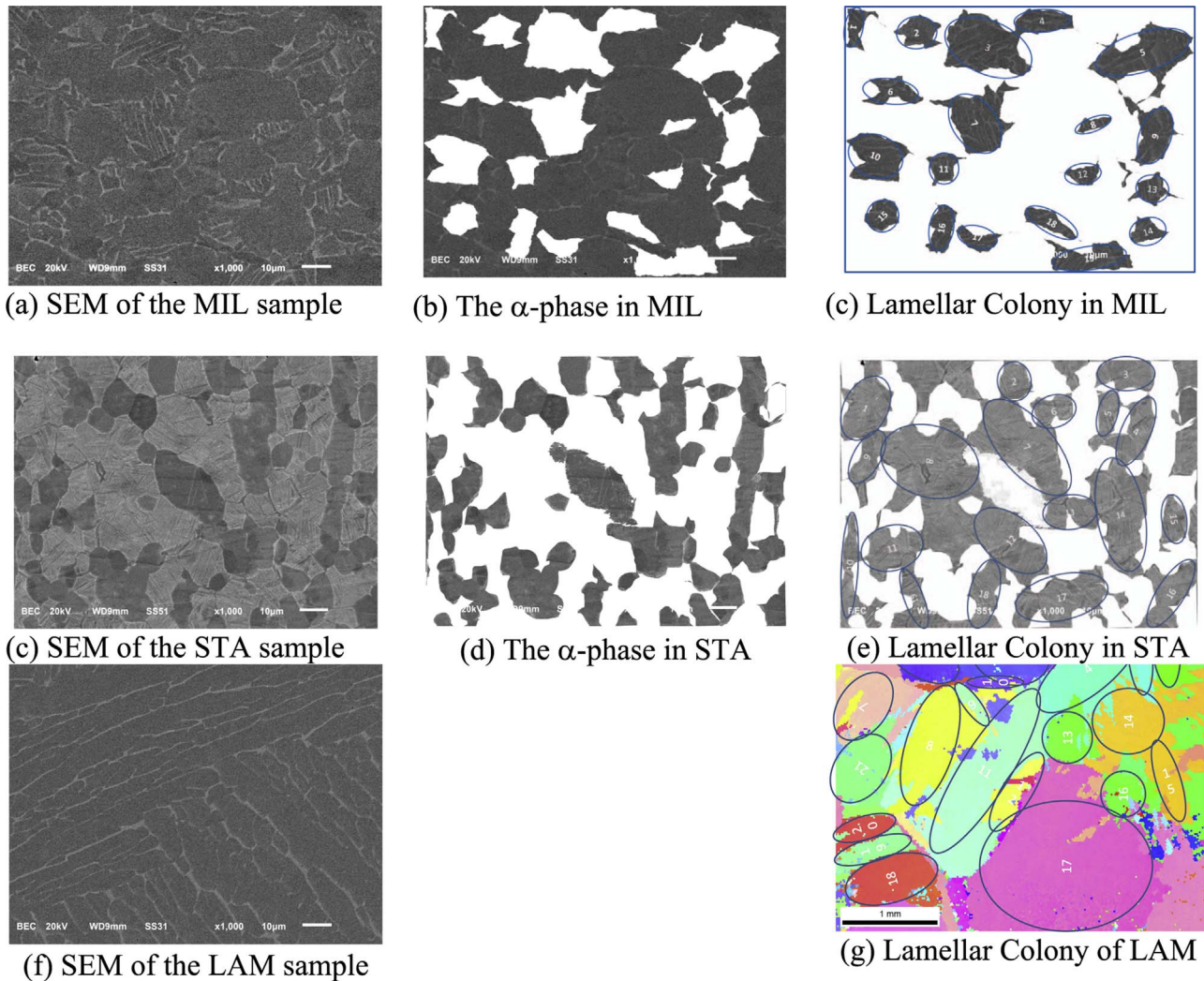
(a) SEM of the MIL sample

(b) The α-phase in MIL

(c) Lamellar Colony in MIL

(c) SEM of the STA sample

(d) The α-phase in STA

(e) Lamellar Colony in STA

(f) SEM of the LAM sample

(g) Lamellar Colony of LAM

Fig. 5. SEM images and elimination of α and lamellar phases in MIL, STA and LAM samples.

Table 6
Microhardness measured on our four samples of Ti64.

Ti64 samples	ELO	MIL	STA	LAM
Ave. hardness (HV)	320.4	308.0	331.9	297.7
Standard derivation	10.7	14.6	6.5	23.0

abrasive, flank wear increased slightly with cutting speed. With 11.9% of the lamellar content in the MIL samples, the flank wear was slightly higher than the ELO sample. However, for the STA sample with the 57.1% lamellar content, the flank wear behavior was much closer to that of the LAM sample which had by far the largest flank wear at the high cutting speed. Flank wear at the low and medium cutting speeds (61 and 91 m/min) slightly increased as the lamellar content increases. However, flank wear was significantly increased at the high cutting speed (122 m/min) with the increase in the lamellar content. The ELO sample contains predominantly the α-phase and the content of the hard α-cluster among three samples, ELO, MIL and STA, are similar. We can conclude that the effect of the hard α-clusters diminishes with the cutting speeds. When comparing the flank wear from MIL, STA and LAM, the effect of the lamellar phase escalates with the cutting speeds. Flank wear can be converted to the flank wear rate by dividing by the cutting distance. Fig. 13 shows the relationships between flank wear rate and the lamellar content in terms of area fraction for four samples. The important finding is that the effect of the hard α-clusters mildly

increases with the cutting speed whereas the effect of the lamellar colonies intensely increases with the cutting speed.

This difference in flank wear can be explained by the microstructural difference between the α-clusters and the lamellar colonies. Kwon [27] and Wong et al. [23] reported the two distinct modes of flank wear depending on the constraint on the abrasive phases, 2-body and 3-body abrasion modes. These are two extreme conditions representing many practical abrasive conditions. In the 2-body abrasion mode, the 'hard' abrasive phases are constrained due to either the complex morphology or the relative large size while abrading the tool material. On the other hand, in 3-body abrasion mode, the 'hard' abrasive phases are not constrained so that the relative motion (e.g.: roll) as third bodies exists between two tribologically interacting bodies. The two distinct modes directly impact how flank wear proliferates in machining. In 2-body abrasion, flank wear increases with the cutting speed while in 3-body abrasion flank wear decreases with cutting speed. The difference is demonstrated on Fig. 14 where the flank wear is represented as a function of temperature (or cutting speed as in most cases the temperature increase with the cutting speed). In machining Ti alloys, flank wear is expected to be the condition of 2-body abrasion but with slight different ramification due to the microstructural difference between the hard α-clusters and the lamella colonies. The complex morphology of the lamellar colonies provides a high level of constraint during abrasive action, which is similar to the extreme case of the 2-body abrasion. The α-crystals surrounding the hard α-clusters do not provide the microstructural constraint for the hard α-clusters (only
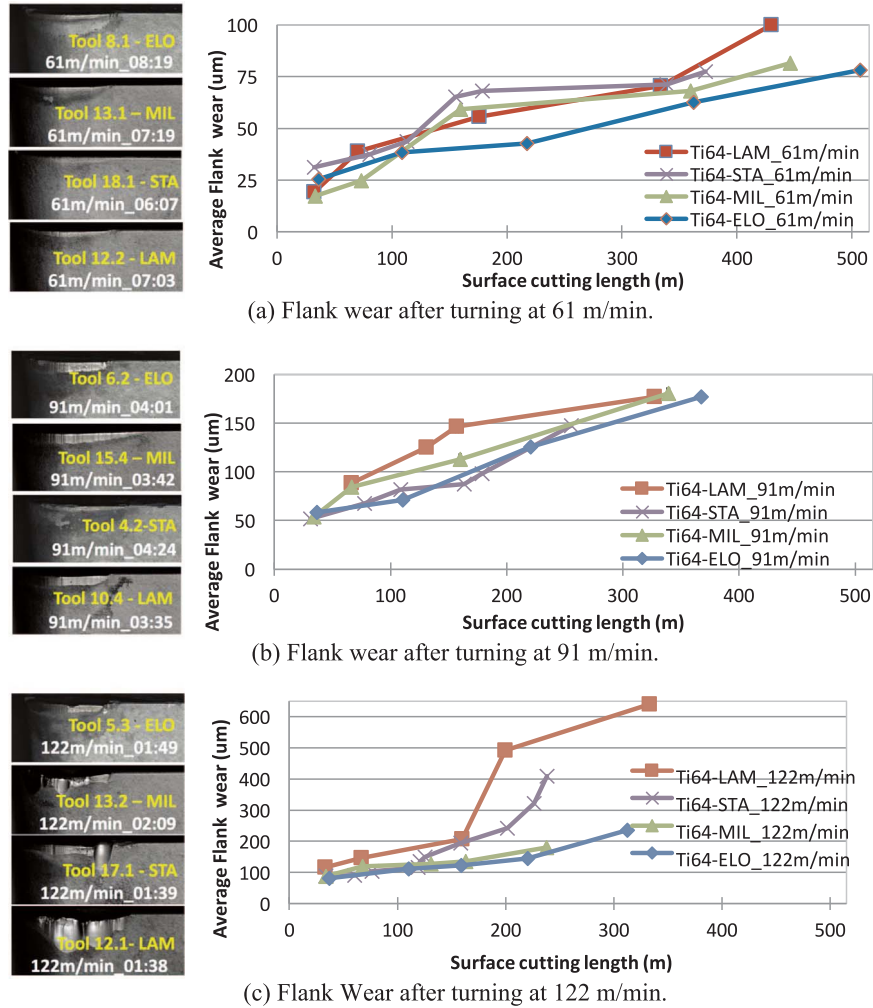
(a) Flank wear after turning at 61 m/min.

(b) Flank wear after turning at 91 m/min.

(c) Flank Wear after turning at 122 m/min.

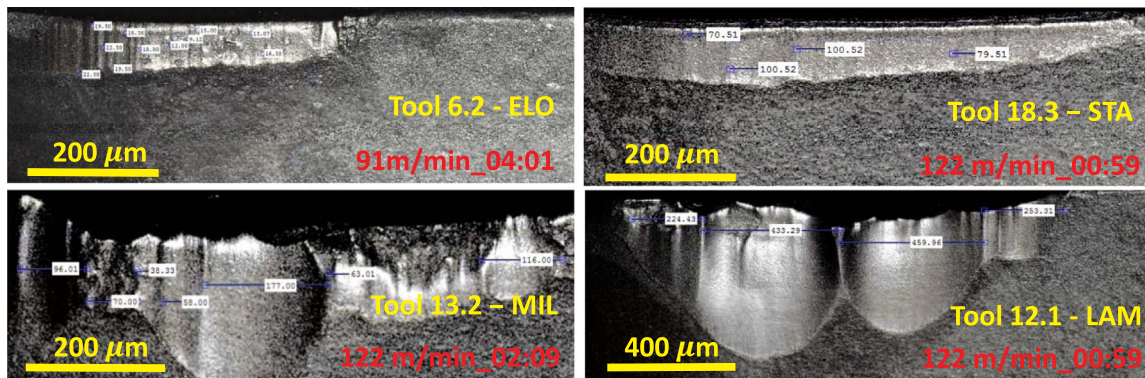**Fig. 6.** Micrographs of flank wear land and the progress of flank wear.

Fig. 7. Measuring the width of each scoring mark on flank wear land after turning at the respective speed in four inserts.
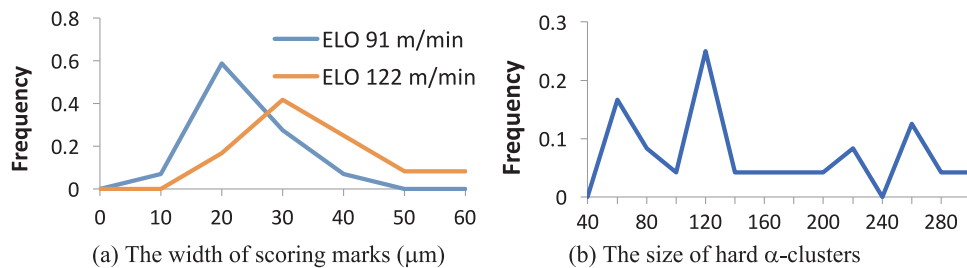

(a) The width of scoring marks (μm)

(b) The size of hard α-clusters

Fig. 8. The histograms of scoring mark width and size of hard α-cluster of the ELO sample.
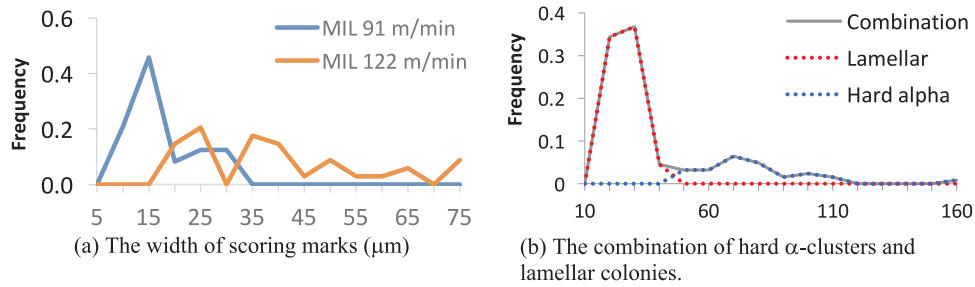
Fig. 9. Histogram representations of the scoring mark, hard α-cluster and lamellar phases of the MIL sample.

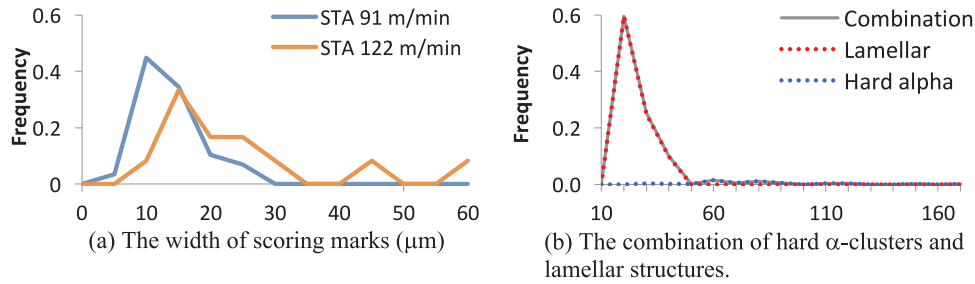Fig. 10. Histogram representations of scoring mark width, hard α-cluster and lamellar colony sizes of the STA sample.
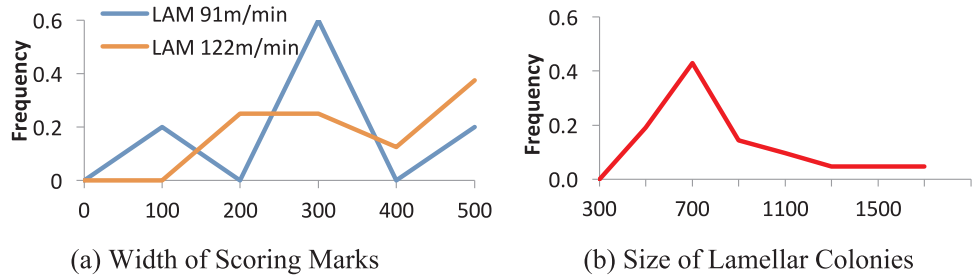

Fig. 11. Histogram representations of scoring marks widths and lamellar colony sizes in the LAM sample.

Table 7
Correlation between microstructural size and scoring mark.

Samples	Scoring mark width (micron)	Hard α-cluster size (micron)	Lamellar size (micron)
ELO	9.1–56	35–201	–
MIL	11.7–54	33–70.2	13.3–38
STA	5–55.5	17–105	12– 31
LAM	96.1–433.3	–	363–1601

Fig. 12. Flank wear as a function of cutting speed.

Fig. 13. Flank wear rate vs lamellar content.
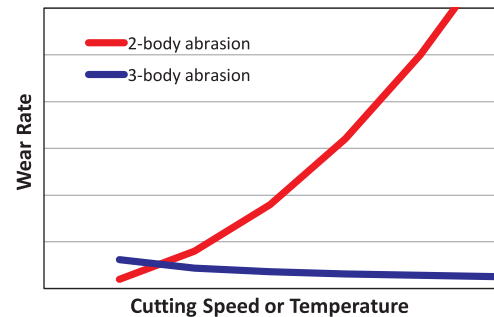
Fig. 14. Difference in wear behavior with 2-body and 3-body abrasion.

3–4% in area fraction) which provide minimal constraints unlike the lamellar phase. As the lamellar content increases gradually with MIL, STA and finally to LAM samples, the complex morphology constraint in the lamellar phase during machining especially at high cutting speeds, which provide the more extreme 2-body abrasion. Therefore, even though the lamellar phase is slightly softer than the α-phase as shown in Table 6, the lamella colonies acts as the more effective abrasives.

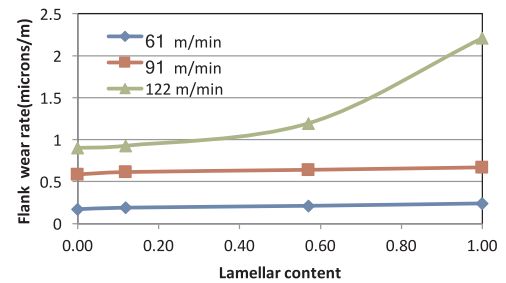The arguments made throughout the paper assumed that the phase

Table 8
Johnson-Cook plasticity models for the mill anneal and lamellar samples.

Sample	A (MPa)	B (MPa)	n	m	C	Ref
Mill annealed	782.7	498.4	0.28	1.0	0.028	Lee et al. [30]
Lamellar	831	858	0.302	0.72	0.015	Chen et al. [31]

Table 9
Flank temperatures at each cutting speed estimated on each sample.

	ELO	MIL	STA	LAM
61 m/min	520 °C	545 °C	620 °C	780 °C
91 m/min	625 °C	660 °C	735 °C	825 °C
122 m/min	715 °C	765 °C	795 °C	830 °C

transformation does not occurred at the flank face. On the crater surface, the temperature reached over 1000 °C even at 60 m/min, which is high enough to transform the material to the β-phase. Also, high stress can also facilitate metastable transformation to the softer β phase, which will revert back to the α-phase when the stress is removed, similar to what happens in dynamic transformation of austenite to ferrite (the softer phase) [28].

To predict the cutting temperature at the flank surface, the Johnson-Cook (J-C) plasticity models has the following form.

$$Y = A\left(1 + \frac{B}{A}\varepsilon^n\right)(1 + C \ln \dot{\varepsilon}')(l - T'^m)$$

where Y is the flow stress, ε is the equivalent flow strain, $\dot{\varepsilon}$ is the non-dimensionalized strain rate and T' is the non-dimensionalized temperature, $T' = (T - T_r)/(T_m - T_r)$ with T_r and T_m are room temperature and melting temperature of Ti64, respectively. The parameters for the J-C models were obtained for the mill annealed [30] and lamellar [31] samples as shown in Table 8. The Arbitrary Lagrangian Eulerian boundaries were applied in Finite Element (FE) Analysis ABAQUS simulation and the element types for the explicit problems with thermal-displacement elements [29]. The detail models including the boundary conditions used can be found in our previous work [24] and the friction coefficient of 0.6 between carbides and Ti64 was applied. The ABQUS simulations were carried out to predict the flank temperature. The flank wear lands in the FE models were 100 μm for the mill annealed sample and 180 μm for the lamellar sample, representing the flank wear observed in our experiments. The temperature of the flank sides were generated by averaging the nodal temperatures on contact area between the tool and work materials through flank wear lands. The temperatures of elongated and solution treated and annealed samples were roughly estimated by interpolating from the temperature results of mill annealed and lamellar samples based on the phase contents. The resulting flank temperature were summarized in Table 9 for all four samples. Based on these results, the transformation to the β-phase (estimated to happen at high 900 °C) does not happen at the flank surface. In addition, our ALE FE model cannot incorporate the segmentation in chip formation, which will reduce the cutting temperature even further.

4. Conclusion

The flank wear behavior after turning four samples of Ti64 (ELO, MIL, STA and LAM as denoted in this paper) was examined. The corresponding area fractions (or content) of the hard α-clusters and the lamellar colonies were obtained by examining the microstructures of the four samples. The lamellar and α contents and their respective sizes vary substantially among the four samples, which enable us to study the relationship between flank wear and both microstructural phases in these samples. This directly links the root causes of the flank wear to be the hard α-clusters and the lamellar colonies in their respective

microstructures. At the low cutting speed (61 m/min), the effect of the hard α-cluster (4% in ELO without any lamellar phase) and the lamellar phase (100% in LAM without any α-phase) are similar in flank wear. As the cutting speed increased, the lamellar phase became much more detrimental in flank wear. At the high cutting speed (122 m/min), the flank wear was about four times higher in the LAM sample compared to those from ELO and MIL samples. The observed wear rates support the wear mechanism of 2-body abrasion, which predicts the wear increases with the temperature. However, the difference in the flank wear behaviors between the hard α-cluster and the lamellar content is astounding, which was attributed to the difference in the microstructural constraints. The alternating phases between α and β in the lamellar colonies offers the more rigid constraints within its microstructure while the hard α-clusters are not as well constrained. This is supported by the much more extensive flank wear by the lamellar phase as the cutting speed (or temperature) increases.

References

[1] C. Leyens, M. Peters, Titanium and Titanium Alloys, Wiley-VCH, Weinheim, 2003.
[2] X. Yang, R.C. Liu, Machining titanium and its alloys, Mach. Sci. Technol. 3 (1) (1999) 107–139.
[3] M.J. Donachie, A Primer on Titanium and Its Alloys. Titanium: A Technical Guide, second ed., ASM International, Materials Park, 2000.
[4] C.N. Elias, J.H.C. Lima, R. Valiev, Ma Meyers, Biomedical applications of titanium and its alloys, J. Miner. Met. Mater. Soc. 60 (3) (2008) 46–49.
[5] E.O. Ezugwu, Z.M. Wang, Titanium alloys and their machinability, J. Mater. Process. Technol. 68 (3) (1997) 262–274.
[6] A.K. Gogia, High-temperature titanium alloys, Def. Sci. J. 55 (2) (2005) 149–173.
[7] H.J. Rack, J.I. Qazi, Titanium alloys for biomedical applications, Mater. Sci. Eng. C 26 (8) (2006) 1269–1277.
[8] G. Lu¨tjering, J.C. Williams, Titanium: Engineering Materials and Processes, Second edition, Springer, Leipzig, 2007.
[9] C. Veiga, J. Davim, A. Loureiro, Properties and applications of titanium alloys: a brief review, Rev. Adv. Mater. Sci. 32 (2012) 133–148.
[10] R. Boyer, G. Welsch, E.W. Collings, ASM Materials Properties Handbook: Titanium Alloys, ASM International, Material Park, 1994.
[11] G. Lütjering, Influence of processing on microstructure and mechanical properties of (α+β) titanium alloys, Mater. Sci. Eng.: A 243 (1) (1998) 32–45.
[12] P.A. Dearnley, A.N. Grearson, Evaluation of principal wear mechanisms of cemented carbides and ceramics used for machining titanium alloy IMI 318, Mater. Sci. Technol. 2 (1) (1986) 47–58.
[13] P.J. Arrazola, A. Garay, L.M. Iriarte, M. Armendia, S. Marya, F. Le Maître, Machinability of titanium alloys (Ti6Al4V and Ti555.3), J. Mater. Process. Technol. 209 (5) (2009) 2223–2230.
[14] N. Khanna, A. Garay, L.M. Iriarte, D. Soler, K.S. Sangwan, P.J. Arrazola, Effect of heat treatment conditions on the machinability of Ti64 and Ti54M alloys, Procedia CIRP 1 (1) (2012) 477–482.
[15] M. Armendia, A. Garay, L.M. Iriarte, P.J. Arrazola, Comparison of the machin-abilities of Ti6Al4V and TIMETAL 54M using uncoated WC-Co tools, J. Mater. Process. Technol. 210 (2) (2010) 197–203.
[16] Y. Kosaka, J.C. Fanning, S.P. Fox, Development of low cost high strength alpha/beta alloy with superior machinability, in: Proceedings of the 10th World Conference on Titanium, 2004, pp. 3028–3034.
[17] A. Attanasio, M. Gelfi, A. Pola, E. Ceretti, C. Giardini, Influence of material microstructures in micromilling of Ti6Al4V alloy, Materials 6 (9) (2013) 4268–4283.
[18] M. Gelfi, A. Attanasio, E. Ceretti, A. Garbellini, A. Pola, Micromilling of lamellar Ti6Al4V: cutting force analysis, Mater. Manuf. Process. 31 (7) (2016) 919–925.
[19] M.J. Bermingham, J. Kirsch, S. Sun, S. Palanisamy, M.S. Dargusch, New observa-tions on tool life, cutting forces and chip morphology in cryogenic machining Ti-6Al-4V, Int. J. Mach. Tools Manuf. 51 (6) (2011) 500–511.
[20] N. Narutaki, A. Murakoshi, S. Motonishi, H. Takeyama, Study on machining of titanium alloys, CIRP Ann. – Manuf. Technol. 32 (1) (1983) 65–69.
[21] N. Narutaki, A. Murakoshi, S. Motonishi, H. Takeyama, Study on machining of titanium alloys, CIRP Ann. – Manuf. Technol. 32 (1) (1983) 65–69.
[22] Z.A. Zoya, R. Krishnamurthy, Performance of CBN tools in the machining of titanium alloys, J. Mater. Process. Technol. 100 (1) (2000) 80–86.
[23] T. Wong, P. Kwon, W. Kim, A predictive model for tool wear on coated inserts, Wear

257 (7–8) (2004) 790–798.

[24] T. Nguyen, P. Kwon, D. Kang, T. Bieler, The root cause of flank wear in turning Ti-6Al-4V with carbides and PCD inserts, J. Manuf. Sci. Eng. 136 (4) (2016) 041018.

[25] T.B. Britton, H. Liang, F.P.E. Dunne, A.J. Wilkinson, The effect of crystal orientation on the indentation response of commercially pure titanium: experiments and simulations, Proc. R. Soc. Lond. A: Math. Phys. Eng. Sci. 466 (2115) (2010) 695–719.

[26] A. Buades, B. Coll, J.M. Morel, A review of image denoising algorithms, with a new one, Multiscale Model. Simul. 4 (2) (2005) 490–530.

[27] P. Kwon, Predictive models for flank wear on coated inserts, J. Tribol. 122 (1) (2000) 340–347.

[28] C. Ghosh, V.V. Basabe, J.J. Jonas, Y.M. Kim, I.H. Jung, S. Yue, The dynamic

transformation of deformed austenite at temperatures above the Ae 3, Acta Mater. 61 (7) (2013) 2348–2362.

[29] Y. Zhang, J.C. Outeiro, T. Mabrouki, On the selection of Johnson-Cook constitutive model parameters for Ti-6Al-4V using three types of numerical models of orthogonal cutting, Procedia CIRP 31 (2015) 112–117.

[30] W.-S. Lee, C.-F. Lin, High-temperature deformation behaviour of Ti6Al4V alloy evaluated by high strain-rate compression tests, J. Mater. Process. Technol. 75 (1) (1998) 127–136.

[31] G. Chen, C. Ren, X. Qin, J. Li, Temperature dependent work hardening in Ti-6Al-4V alloy over large temperature and strain rate ranges: experiments and constitutive modeling, Mater. Des. 83 (2015) 598–610.